

Structural characterization of the candidate Weyl semimetal CeGaGeLiam J. Scanlon¹,[✉] Santosh Bhusal,¹ Christina M. Hoffmann,² Junhong He,² Sean R. Parkin,³
Brennan J. Arnold,¹ and William J. Gannon^{1,*}¹*Department of Physics and Astronomy, University of Kentucky, Lexington, Kentucky 40506, USA*²*Neutron Scattering Division, Oak Ridge National Laboratory, Oak Ridge, Tennessee 37831, USA*³*Department of Chemistry, University of Kentucky, Lexington, Kentucky 40506, USA* (Received 9 December 2024; revised 21 April 2025; accepted 28 April 2025; published 12 May 2025)

Weyl semimetals have a variety of intriguing physical properties, including topologically protected electronic states that coexist with conducting states. Possible exploitation of topologically protected states in a conducting material is promising for technological applications. Weyl semimetals that form in a noncentrosymmetric structure that also contain magnetic moments may host a variety of emergent phenomena that cannot be seen in magnetic, centrosymmetric Weyl materials. It can be difficult to distinguish definitively between a centrosymmetric structure and one of its noncentrosymmetric subgroups with standard powder x-ray diffractometers in cases where two atoms in the compound have nearly the same atomic number, as is the case for the candidate Weyl semimetal CeGaGe. In these cases, a careful single-crystal neutron diffraction experiment with high-angle reflections provides complimentary information to x-ray diffraction and definitively resolves any ambiguity between centrosymmetric and noncentrosymmetric crystal structures. Single-crystal neutron diffraction measurements on the candidate Weyl semimetal CeGaGe confirms that its structure is noncentrosymmetric, described by space group 109 ($I4_1md$) rather than the centrosymmetric space group 141 ($I4_1/amd$). There are many high-angle reflections in the dataset that give clear, physically intuitive evidence that CeGaGe forms with $I4_1md$ symmetry since Bragg planes of these reflections can contain Ga with no Ge or vice versa, whereas the Bragg planes for a structure with $I4_1/amd$ symmetry would have a mix of Ga and Ge. Further, in some crystals we have studied, there is clear evidence for a structural transition from body-centered $I4_1md$ symmetry to primitive $P4_3$ and/or $P4_1$ symmetry.

DOI: [10.1103/PhysRevB.111.184102](https://doi.org/10.1103/PhysRevB.111.184102)**I. INTRODUCTION**

The recent appreciation for the role of topology in condensed matter physics has driven the study of materials that host protected electronic states due to their potential uses in next-generation technologies [1–6]. Among bulk materials that potentially host such states, Weyl semimetals also feature conducting states in their bulk, allowing for the exploitation of both protected and conventional electronic states in future applications. For candidate Weyl materials, it is critical to have a detailed understanding of the underlying symmetries in the material, as these properties govern whether or not Weyl points in the electronic band structure can exist at all and what properties these Weyl points may possess. For a Weyl semimetal to exist, there must be either ordered magnetic moments that break time-reversal symmetry (TRS) [7] or broken inversion symmetry in the crystal structure [8]. When combined with spin-orbit coupling, these broken symmetries can lead to degenerate bands that are topologically protected with linear dispersions that mimic Weyl particles [4–6]. Some exotic topological states—for instance, lines of Weyl points in the band structure known as Kramers nodal lines—can only exist in materials with broken inversion symmetry [9,10].

Given that the physical properties observed in experiments on correlated topological matter are intricately linked to the underlying symmetries of the material, it is absolutely critical to have an understanding of these symmetries. For a potential Weyl material, the presence or lack of TRS can be found through measurements of thermodynamic properties to determine whether a material is in a magnetically ordered state in a certain temperature range. However, the presence or lack of inversion symmetry can be a much more subtle detail, as it relates to the intricacies of a crystal structure, and determinations are also complicated by the elements that make up the material.

Regardless, in some instances, materials with Weyl points in their band structures possess both magnetic moments that order, breaking TRS, and noncentrosymmetric crystal structures. In such materials, it is possible to have Weyl states above the magnetic ordering temperature and study the interplay of Weyl quasiparticles with magnetic ordering. One such family of materials with noncentrosymmetric crystal structures that have been studied in this context are the RXZ materials where R is a rare-earth element, X is Al or Ga, and Z is Si or Ge. There are at least 12 known materials in this family [8,11–61]. When the rare-earth element is La, there are no magnetic moments, and TRS is preserved [8, 37–39]. When the rare-earth element is Ce, Pr, Nd, Sm, or Gd, the materials order magnetically and break TRS below the

*Contact author: wgannon@uky.edu

ordering temperature [11–36,40–61]. As single crystals, each member of this family has tetragonal, noncentrosymmetric $I4_1md$ symmetry (space group 109).

A wide variety of physics is found in this material family. For instance, in NdAlSi, the ordered magnetic structure is helical, with an incommensurate ordering vector that matches the nesting of the Weyl nodes in the band structure [11]. In CeAlGe, the magnetic order is a long-wavelength meron-antimeron type order, where the topology of the order can be tuned with magnetic field while simultaneously changing the magnitude of the observed topological Hall effect [22]. In CeAlSi, the positions of the Weyl nodes move in reciprocal space with the onset of magnetic order [34]. In PrAlSi, a magnetic field-induced Lifshitz transition has been observed [53].

Several of these materials were first identified not as high-quality single crystals but rather in polycrystalline form. For example, CeAlGe and NdAlSi were both first produced as polycrystals via arc-melting [62–64]. In these instances, the materials were reported to be alloys, with symmetry given as $I4_1/amd$ (space group 141) based on powder x-ray diffraction (PXRD) measurements.

The difference between $I4_1md$ and $I4_1/amd$ in the context of these materials is the positioning of the X and Z atoms in the structure. With noncentrosymmetric $I4_1md$ symmetry, the X and Z atoms occupy distinct crystallographic sites (with Wyckoff site symmetry $4a$), shown in Figs. 1(a) and 1(c) for the material CeGaGe, the subject of this paper. With $I4_1/amd$ symmetry, the X and Z atoms would need to randomly occupy the same crystallographic site (with site symmetry $8e$) with 50% occupancy, restoring inversion symmetry in the structure [Figs. 1(b) and 1(d)].

In arc-melted samples, the random polycrystalline $I4_1md$ grains would be practically indistinguishable from an $I4_1/amd$ alloy in a PXRD experiment, especially due to the possibility of inversion twinning with the $I4_1md$ symmetry. Since the band structure in a material is intimately linked to the crystal structure, it is critical to have an accurate structure determined from high-quality single crystals to fully understand the emergent physics. In the case of CeAlGe, this was done with careful single-crystal x-ray diffraction (SCXRD) since the atomic scattering factors of Al and Ge are significantly different [19,65]. For NdAlSi, a careful single-crystal neutron diffraction (SCND) experiment was performed due to the similarities in the x-ray atomic scattering factor of Al and Si [11,65].

The subject of this paper CeGaGe is also a member of the RXZ family. Authors of early reports on arc-melted samples determined the crystal structure to have $I4_1/amd$ symmetry from PXRD [66,67]. In CeGaGe, ferromagnetic order was seen at $T_C = 5.5$ K, with a Sommerfeld coefficient $\gamma = 40$ mJ/mol K² [68], significantly larger than in CeAlGe ($\gamma = 0.93$ mJ/mol K²) [19], suggesting enhanced electronic correlations. Authors of a more recent report on single crystals of CeGaGe grown from flux have confirmed the magnetic ordering at $T_C = 5.5$ K but found a considerably smaller Sommerfeld coefficient $\gamma = 13$ mJ/mol K² [69]. Authors of all of these reports have confirmed that CeGaGe is a poor metal, with a residual resistivity ratio as high as 2 in the likely higher-quality flux-grown crystals.

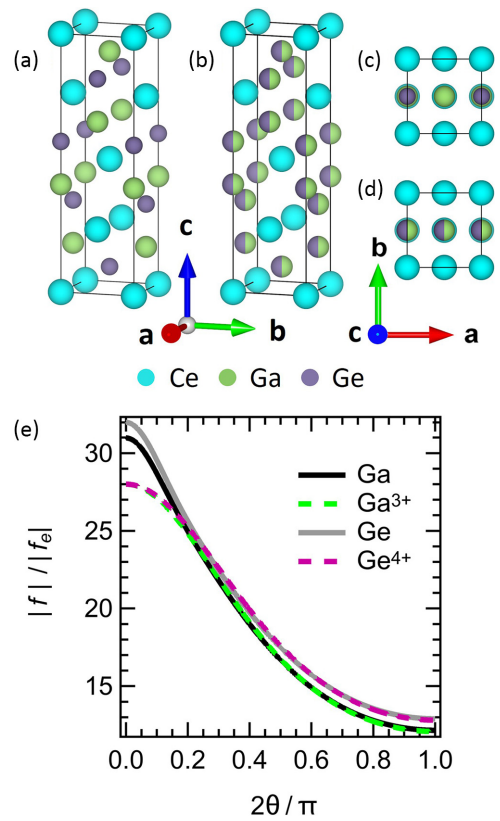


FIG. 1. Structure of CeGaGe: The unit cell of CeGaGe given (a) $I4_1md$ and (b) $I4_1/amd$ symmetries. Ce (cyan), Ga (green), and Ge (purple) are shown. For the $I4_1md$ space group, Ga and Ge occupy distinct crystallographic sites, each with Wyckoff symmetry $4a$. For the $I4_1/amd$ space group, Ga and Ge are shown as a random mixture on the crystallographic site with Wyckoff symmetry $8e$. Structures with the same (c) $I4_1md$ and (d) $I4_1/amd$ symmetries are shown projected along the crystal c axis. (e) The normalized x-ray atomic scattering factors as a function of scattering angle 2θ are shown for elemental Ga (black solid line) and Ge (gray solid line) as well as the common Ga^{3+} (green dashed line) and Ge^{4+} (magenta dashed line) oxidation states calculated using the method prescribed in Ref. [65].

The central problem is that there has not yet been a definitive structural determination for CeGaGe. This is not possible using standard powder x-ray characterization tools available at most institutions. As discussed above, structural determination would not have been possible in early polycrystalline samples with PXRD. However, even a PXRD experiment on a sample made from crushed single crystals would struggle to determine the structure in the RXZ materials because of the random orientation of the powder grains. It was shown that PXRD data from flux-grown single crystals of CeGaGe fits well to a model with $I4_1md$ symmetry [69], but a side-by-side comparison of refinements to models with $I4_1md$ and $I4_1/amd$ symmetries has not been made. PXRD data collected from a sample made from crushed single crystals is shown in Figs. 2(a) and 2(b). Rietveld refinements [70] using models with $I4_1md$ [Fig. 2(a)] and $I4_1/amd$ [Fig. 2(b)] symmetries are virtually identical and give equivalently good descriptions of the data. This is discussed further in Sec. II. In CeGaGe

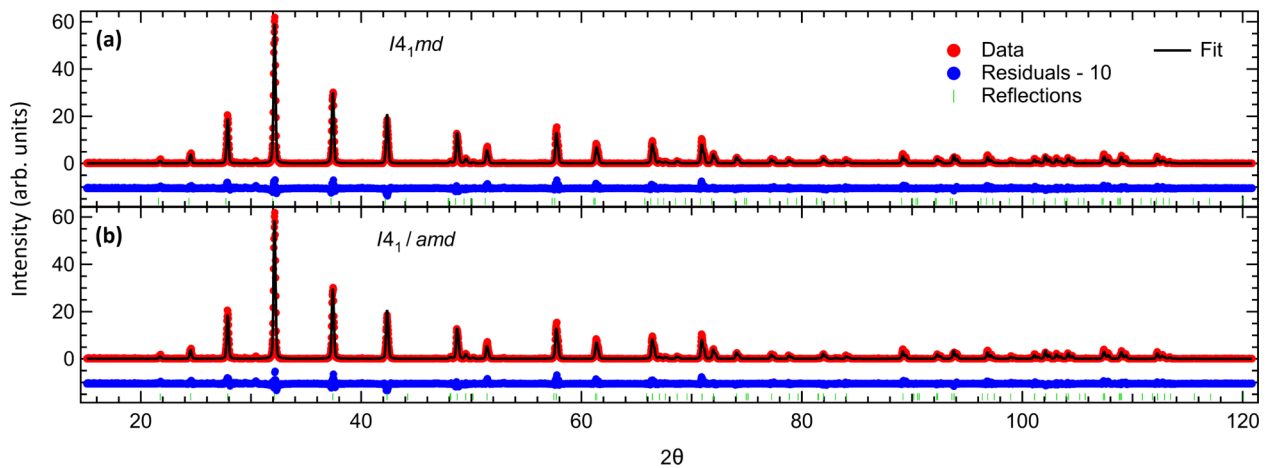


FIG. 2. Powder x-ray diffraction (PXRD): Scattered x-ray intensity as a function of scattering angle 2θ measured by PXRD (red) and calculated by Rietveld refinements (black) to models with (a) $I4_1md$ and (b) $I4_1/amd$ symmetries. Refinements are nearly identical in both panels. Expected positions of Bragg reflections (green hatches) and offset residuals (blue) for each fit are shown. These refinements are virtually indistinguishable.

specifically, SCXRD is complicated by the similarities of x-ray scattering factors for Ga and Ge. The x-ray scattering factors for Ga, Ge, and their common oxidation states are plotted in Fig. 1(e). There is little difference between Ga and Ge across 180° in scattering angle 2θ . A single-crystal structural determination avoiding the powder grain issue that also uses a complimentary technique to increase the contrast between the Ga and Ge sites would definitively determine the structure when combined with PXRD and SCXRD measurements that can be made at many institutions.

This same issue was faced with the material NdAlSi, where the similarity of Al and Si in XRD measurements made structural determination difficult, even with high-quality single crystals [11]. For that material, the structure was definitively determined to have $I4_1md$ symmetry using SCND. Al and Si have significantly different coherent neutron scattering lengths [71,72], making SCND a straightforward way to determine the structure.

We have performed a similar SCND experiment on CeGaGe as well as a number of SCXRD experiments. We find that the structure has $I4_1md$ symmetry in all samples. However, we also find in some samples that there is a subtle structural transition away from the body centered $I4_1md$ to the primitive, noncentrosymmetric $P4_3$ (and/or $P4_1$) symmetry upon decreasing temperature. These results lay a foundation for understanding the broader picture of magnetic and potential Weyl physics in CeGaGe and emphasizes that extreme caution in structural determination is needed in this family of materials.

II. CRYSTAL SYNTHESIS AND CHARACTERIZATION

Elemental Ce (Aldrich 99.9%), Ga (Aesar 99.99999%), and Ge (Aldrich 99.9999%) in the molar ratio 0.86:1.0:0.79 were arc-melted into two rods ~ 3 inches each in length. The melted material in each rod was cut, mixed, and remelted several times to ensure compositional homogeneity. These polycrystalline rods were then mounted and coaligned in a Quantum Designs two-mirror floating-zone furnace. Floating-

zone refinement was done under a 3 bar argon atmosphere to minimize loss of Ga and Ce due to their relatively high vapor pressures. While the crystal was being grown, there was a 4 scf/h flow of Ar through the system to minimize vapor plating to the walls of the growth chamber between the samples and mirrors. Growth was done at a rate of 8 mm/h, and each rod was rotated in opposite directions with a frequency of 5 rpm. This yielded a crystal of ~ 2.5 cm in length and 1.7 g in mass.

Energy dispersive x-ray spectroscopy (EDX) was used to determine composition of the sample. EDX spectra were taken at 38 sites on the sample using a Quanta FEG 250 environmental scanning electron microscope (SEM) equipped with an Oxford Instruments XSTREAM2 EDX detector. Each spectrum was collected with $\sim 500\,000$ photon counts. A representative spectrum can be found in Fig. S-2 in the Supplemental Material [73]. Data were analyzed with the Oxford Instruments AZtec data suite using 20 keV range, 2048 channels, and pulse pile-up correction [74]. Carbon from the SEM mounting tape, aluminum from the interior of the SEM chamber, and any possible residual oxygen were included in fits to spectra but not included in calculating molar compositions of the elements. Ce, Ga, and Ge showed molar ratio 0.95:1.0:0.86, as can be seen in Table I. All spectra

TABLE I. Composition of CeGaGe: The composition of the CeGaGe floating-zone refined crystal determined by EDX and by SCND refinements to models with $I4_1md$ and $I4_1/amd$ symmetries. The compositions from EDX data and refinement with $I4_1md$ symmetry are within uncertainty of each other.

	Composition of $Ce_\alpha Ga_\beta Ge_\gamma$		
	α (Ce)	β (Ga)	γ (Ge)
EDX	0.95(2)	1.000(9)	0.86(1)
$I4_1md$	0.91(2)	1.00(2)	0.83(2)
$I4_1/amd$	0.93(4)	0.96(2)	1.00(8)

were normalized to a maximum composition of 1, with other compositions adjusted accordingly.

To confirm that models with $I4_1md$ and $I4_1/amd$ symmetries cannot be distinguished with PXRD tools, we performed an experiment using a powder prepared from the floating-zone refined crystal. Measurements were made with a Bruker D8 Advance diffractometer equipped with a Göbel mirror and Soller slits for beam collimation and nickel filter to suppress $K\beta$ radiation. The results of the measurements are shown in Fig. 2. Rietveld refinements [70] to models with $I4_1md$ and $I4_1/amd$ symmetries using the FULLPROF Suite analysis package [75] are virtually identical. The reported χ^2 values are 1.05 for $I4_1md$ and 1.08 for $I4_1/amd$. The reliability factor R_{wp} was 18.7 for $I4_1md$ and 19.0 for $I4_1/amd$. Details of the refined structures can be seen in Table S-I in the Supplemental Material [73].

III. SCND DATA ACQUISITION AND ANALYSIS

A high-resolution neutron diffraction experiment with sufficient reciprocal space coverage can accurately determine whether CeGaGe has $I4_1md$ or $I4_1/amd$ symmetry. The bound coherent neutron scattering lengths for Ga and Ge differ by 12% [71,72], making neutron scattering quite sensitive to differences in Ga and Ge. A single-crystal experiment eliminates the randomization of the crystal grains, while an experiment with large reciprocal space coverage can resolve features at particularly small length scales.

A SCND experiment was done using the TOPAZ diffractometer at the Spallation Neutron Source at Oak Ridge National Laboratory [77]. A crystal with mass 3.37 mg and roughly spherical shape with radius 0.3 mm cut from our floating-zone grown crystal was chosen for the experiment. The sample was mounted with random orientation onto an aluminum sample holder pin with glue, as is typical for TOPAZ experiments. The sample and pin were wrapped with pure Al foil to ensure good thermal contact and loaded into a closed cycle refrigerator on the instrument and cooled to $T = 100$ K. The orientation of the sample was varied by rotating around the vertical axis, and data were collected for 19 different rotation angles ϕ . At each angle, data were collected for ~ 50 min as the sample was exposed to a white beam of neutrons. The wavelengths of the scattered neutrons were resolved by time of flight (TOF).

From these measurements, the crystal unit cell was determined to be tetragonal with $a = b = 4.2708(1)$ Å and $c = 14.5480(4)$ Å. All reciprocal space scattering data are indexed in reciprocal lattice units (r.l.u.). A representative plot of the data in the $k = 0$ reciprocal space plane is shown in Fig. 3. Measurements from all 19 rotation angles merged well, and all diffraction peaks appear at integer reciprocal lattice indices, indicating a high-quality single-crystal sample. The $k = \pm 1$ planes are shown in Fig. S-3 in the Supplemental Material [73] to further illustrate data quality.

The raw TOF data were reduced using MANTID reduction scripts for TOPAZ measurements [78,79]. The reduction normalizes the data, accounting for absorption, neutron flux, solid angle, Lorentz factor, background, and outliers. The reduced data give the structure factor for each observed Bragg reflection in arbitrary units. For both structures, 4430 Bragg

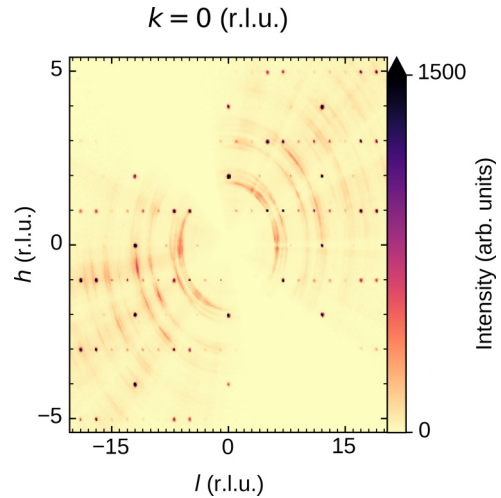


FIG. 3. The $k = 0$ plane of the merged single-crystal neutron diffraction (SCND) data before normalization. The data for the 19 different ϕ angles merged well, showing reflections only at integer indices in reciprocal space which are consistent with the reflection conditions for $I4_1md$ and $I4_1/amd$ symmetries [76].

reflections were indexed. Each of the structure factors had square modulus $|F_o|^2$ and uncertainty σ_o^2 such that $|F_o|^2/\sigma_o^2 \geq 3$, which is larger than the forced signal to noise cutoff of $|F_o|^2/\sigma_o^2 \geq 1$.

Structural refinement was performed using GSAS-II [80] software. Scale, atomic position, anisotropic thermal parameters, occupancy, and extinction were refined for models with $I4_1md$ and $I4_1/amd$ symmetries. When the refinement is carried out with site exchange in a model with $I4_1md$ symmetry, there is $< 3\%$ site exchange between Ga and Ge, with uncertainty on the order of 10%, and so the crystallographic information reported here is from a refinement that does not include site exchange. Calculated structure factors using both the $I4_1md$ and $I4_1/amd$ space groups agree reasonably well with observed structure factors, as can be seen in Figs. 4(a) and 4(c). When $|F_o|^2$ is plotted as a function of the refined, calculated structure factors $|F_c|^2$, in both models, the result is a dataset that is tightly grouped to a line of slope 1 passing through the origin, indicating that the refinements $|F_c|^2$ are good descriptions of our observation $|F_o|^2$. Indeed, for the strongest reflections, there is little difference between the two crystal structures in question.

However, the reliability factors (R) for the two structural models are significantly different, where R is given by

$$R = \frac{\sum |F_o| - |F_c|}{\sum |F_o|}, \quad (1)$$

where F_o and F_c are the observed and calculated structure factors, respectively. Here, $R = 0.161$ for $I4_1md$ and $R = 0.224$ for $I4_1/amd$, a difference of 32.7%, suggesting that $I4_1md$ is a significantly better description of the measurements. The goodness-of-fit value of 19.13 for $I4_1md$ is lower than that of 22.40 for $I4_1/amd$ by 15.7%. The main difference in the refinements for the two structural models is seen in the weakest Bragg reflections. When the same data from Figs. 4(a) and 4(c) are plotted on a log-log scale to emphasize the weakest

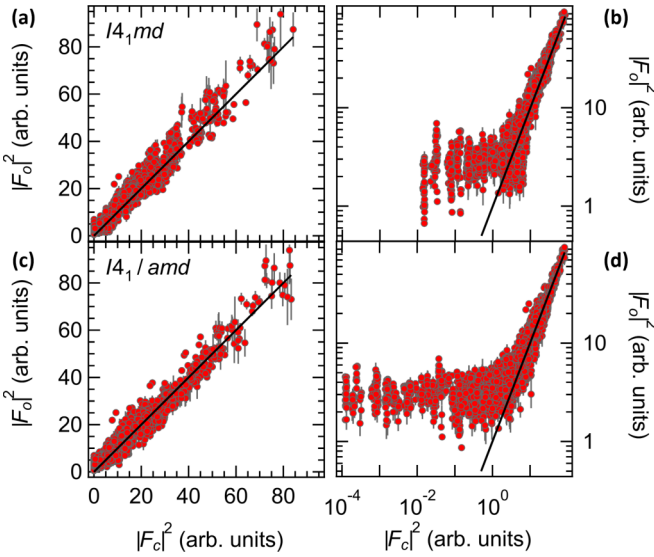


FIG. 4. Single-crystal neutron diffraction (SCND) refinements: Square moduli of observed vs square moduli of calculated structure factors for space groups (a) $I4_1md$ and (c) $I4_1/amd$. The solid black lines have slope 1 and pass through the origin. Plots (b) and (d) are the same plots as (a) and (c), respectively, but on a log-log scale.

reflections [Figs. 4(b) and 4(d)], it is clear that there are a number of peaks that are not well described by a model with $I4_1/amd$ symmetry.

This is not simply an artifact of plotting on a log-log scale. There are 1236 data points where $10^{-4} \leq |F_c|^2 \leq 1.25$ for the $I4_1/amd$ space group. Each of these reflections in the $I4_1/amd$ dataset indexed by hkl with rotation angle ϕ , can be plotted against the corresponding reflection in the $I4_1md$ dataset indexed by the same hkl and ϕ . For 986 of the 1236 reflections, $I4_1md$ predicts more intensity than $I4_1/amd$, putting 911 of the 1236 measured $|F_o|^2$'s in better agreement with the $I4_1md$ structural model.

The scattering vectors for these 1236 data points have relatively large magnitudes, as can be seen in Fig. 5(b). Since magnitudes in reciprocal space are generally inversely

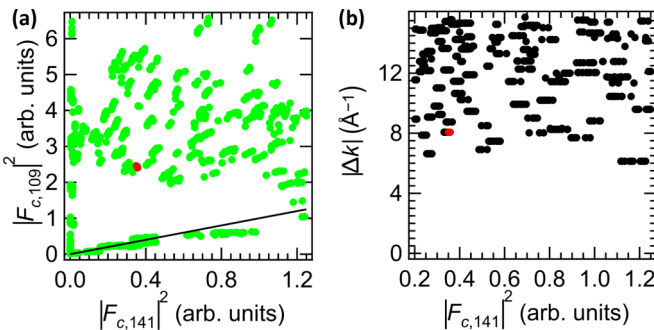


FIG. 5. Reflections with small $|F_c|^2$: (a) $|F_c|^2$ for the $I4_1md$ space group vs corresponding $|F_c|^2$ for $I4_1/amd$ for common Bragg reflections appearing at the same ϕ . The black line has a slope of 1 and passes through the origin. (b) Magnitude of scattering vector as a function of $|F_c|^2$ for $I4_1/amd$. In both (a) and (b), points indexed by $h, k, l = -2, -2, -16$ are highlighted in red since this reflection is shown in Fig. 6 as an example of a high quality, weak reflection.

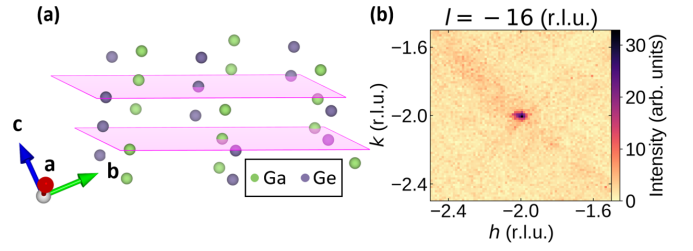


FIG. 6. (a) The crystal structure with $I4_1md$ symmetry without Ce atoms, showing Ga in green and Ge in purple. Lattice planes with indices $(-2, -2, -16)$, corresponding to one of the Bragg reflections where the structure factors for the $I4_1md$ and $I4_1/amd$ models differ most, are shown. (b) Plot of the $(-2, -2, -16)$ peak in reciprocal space, indicating that, although a weak reflection, it is clearly distinguishable from the background scattering.

proportional to magnitudes in real space, this suggests that the reflections where $I4_1md$ provides a significantly better description are representative of structure at short length scale. Indeed, the distance between Ga and its nearest neighbor Ge is 2.417 Å, which is a short length scale.

Closer examination of these reflections reveals how important they are in the structural determination. Example Bragg planes for one of the reflections in Fig. 5, the $(-2, -2, -16)$ peak, can be seen in Fig. 6(a), along with a plot of the $(-2, -2, -16)$ peak in reciprocal space, Fig. 6(b). Although this is a weak peak, it has good signal to noise and is considerably stronger than the Al background that surrounds it. Considering that the Bragg plane for $(-2, -2, -16)$ can have Ga atoms with no Ge atoms or vice versa for the $I4_1md$ space group but would include both Ga and Ge for $I4_1/amd$, it is physically intuitive why the intensities of these peaks are predicted to be significantly lower for the $I4_1/amd$ model. A common feature of the data points in Fig. 5 is that they appear at relatively large scattering vectors and come from Bragg planes that would contain only Ga or Ge for $I4_1md$ but would contain a mix of Ga and Ge for $I4_1/amd$.

All of the refined quantities for the correct $I4_1md$ model except for the scale factors are shown in Table II. The unit cell parameters are in excellent agreement with previous reports [66,67,69]. The average of the anisotropic thermal parameters is smaller than the isotropic thermal parameters reported in Ref. [66]. This is expected, given that the present experiment was done at $T = 100$ K, while the experiment in Ref. [66] was done at room temperature.

IV. SCXRD

A complimentary single-crystal x-ray scattering measurement can give further structural information, especially since Friedel's law prevents observation of inversion twinning without resonant scattering, and none of the elements in CeGaGe have resonant effects in the thermal neutron range [81,82]. The only merohedric twin law allowed for $I4_1md$ is inversion twinning, which is distinguishable in a SCXRD experiment due to resonant scattering of electrons. Moreover, the relative ease of a SCXRD experiment in a local laboratory would allow for far more rapid structural analysis of new samples grown under different conditions going forward.

TABLE II. Crystallographic information of the CeGaGe structure for $I4_1md$ refinement: The anisotropic thermal parameter $U_{1,1}$ is proportional to the mean square displacement of the atom along the a axis, $U_{2,2}$ is proportional to the mean square displacement of the atom along the b axis, and $U_{3,3}$ is proportional to the mean square displacement along the c axis. The secondary type-1 extinction parameter E_g was 5.22×10^{-4} .

Atom	x	y	z	Occ.	$U_{1,1}$	$U_{2,2}$	$U_{3,3}$
Ce	0.0	0.0	0.000	0.91(2)	0.0038(8)	0.010(1)	0.0077(7)
Ga	0.0	0.0	0.4171(1)	1.00(2)	0.0031(3)	0.0146(7)	0.0011(4)
Ge	0.0	0.0	0.5829(1)	0.83(2)	0.019(1)	0.019(1)	0.013(1)

A small grain of the sample used for SCND was used to conduct a SCXRD experiment. Data were collected at $T = 100$ K on a Bruker D8 Venture κ -axis diffractometer using molybdenum $K\alpha$ x-rays with nitrogen gas stream for cooling. Raw data were integrated, scaled, merged, and corrected for Lorentz-polarization effects using the APEX3 package [83]. Corrections for absorption were applied using SADABS [84]. The structure was solved by iterative dual-space methods (SHELXT [85]), and refinement was carried out against square moduli of observed structure factors by weighted full-matrix least-squares (SHELXL [86]). All atoms were refined with anisotropic displacement parameters. Crystallographic parameters of the determined structure are summarized in Table S-II in the Supplemental Material [73].

The crystallographic reliability factors, defined by Eq. (1), are superior for refinements using $I4_1md$ vs $I4_1/amd$ symmetry, giving $R = 0.0249$ for $I4_1md$ and $R = 0.0263$ for $I4_1/amd$. The goodness-of-fit values are 1.146 for $I4_1md$ and 1.258 for $I4_1/amd$.

Given all of these results, the SCXRD analysis corroborates the SCND analysis, and $I4_1md$ symmetry is the correct description for this CeGaGe sample. Analysis of the SCXRD data with this symmetry give a Flack parameter [87] of 0.49(8). The small uncertainty of the Flack parameter indicates that the parameter is well defined, and so the structure is noncentrosymmetric. The Flack parameter being ~ 0.5 indicates that there is nearly perfect inversion twinning in the sample.

These SCXRD results are plotted in Fig. 7 in a fashion like the SCND presentation (Fig. 4). The discrepancies between data and refinements in Figs. 7(b) and 7(d) are not nearly as pronounced as they are in the the SCND analysis, Figs. 4(b) and 4(d). When combined, SCND and SCXRD give a more complete picture of the crystal structure of CeGaGe.

V. STRUCTURAL PHASE TRANSITION IN OTHER CeGaGe SAMPLES

Given the relative scarcity of neutron scattering time on a high-resolution diffractometer and reasonable agreement between our SCND and SCXRD results, SCXRD was used to determine the structure of additional CeGaGe crystals. As discussed above, the crystal that was used on the TOPAZ diffractometer was found to have I -centered $I4_1md$ tetragonal symmetry at $T = 100$ K in the SCND experiment and at $T = 100$ K in the SCXRD experiment. Additional SCXRD measurements confirm that this is the correct symmetry at room temperature for this sample.

However, a crystal synthesized using the flux-growth technique [88,89] using the same recipe as in Ref. [69] shows a transition from I -centered to a primitive tetragonal symmetry, as can be seen in Fig. 8. When this sample is measured with SCXRD at room temperature, all Bragg reflections that are observed can be indexed with reflections that are expected for $I4_1md$ symmetry. As an example, the $k = 1$ Bragg plane is shown in Fig. 8(a), where only expected reflections are observed. When the sample is cooled to $T = 100$ K and the measurement is repeated [Fig. 8(b)], weak Bragg reflections appear that are not allowed for $I4_1md$ symmetry. These additional reflections are consistent with a transition to a primitive tetragonal structure.

SCXRD refinement shows that the structure of the flux-grown sample is well described with chiral $P4_3$ symmetry (space group 78). A Flack parameter of 0.44(8) indicates a mix of $P4_3$ and its enantiomer $P4_1$ (space group 76) since point inversion of a chiral structure transforms it to its enantiomer [90,91]. Crystallographic information for the refinement to the $P4_3$ structure can be found in Table S-III in the Supplemental Material [73].

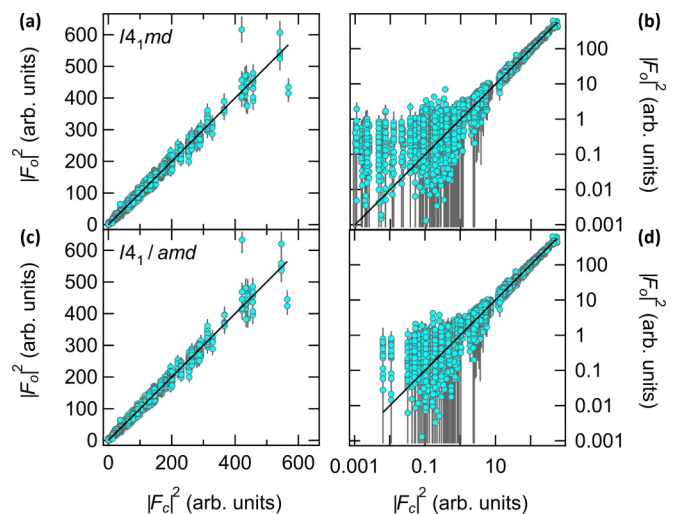


FIG. 7. Square moduli of observed structure factors measured with single-crystal x-ray diffraction (SCXRD) vs square moduli of calculated structure factors for space groups (a) $I4_1md$ and (c) $I4_1/amd$. Solid black lines have slope 1 and pass through the origin. Plots (b) and (d) are the same plots as (a) and (c), respectively, but on a log-log scale. There are 181 data points where $0.001 < |F_c|^2 < 0.0064$ for $I4_1md$. For each of these 181 data points, all data points with matching hkl indices for the $I4_1/amd$ dataset have $|F_c|^2 = 0$.

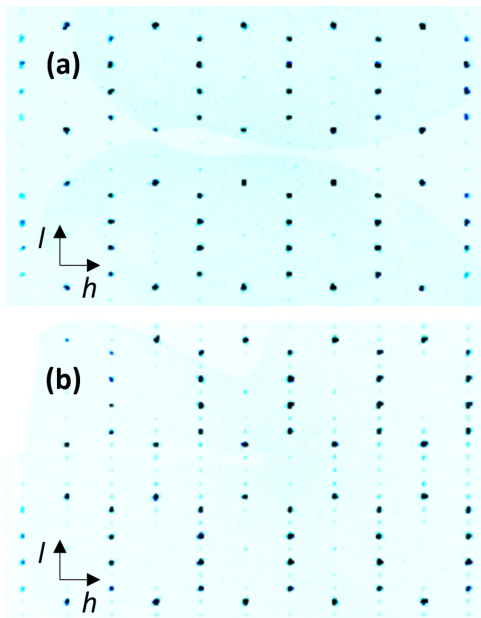


FIG. 8. Evidence of structural transition in flux-grown CeGaGe obtained with single-crystal x-ray diffraction (SCXRD). (a) The $k = 1$ plane at room temperature. Intensity is on a linear scale and contrast has been enhanced to show weaker peaks more clearly. The l axis is vertical, and the h axis is horizontal. (b) The $k = 1$ plane at 100 K. The appearance of additional weak peaks indicates that the structure has transitioned from the body-centered tetragonal $I4_1md$ structure to the primitive tetragonal $P4_1$ or $P4_3$ structure.

The difference between $I4_1md$ and $P4_3$ (or $P4_1$) is extremely subtle in this context. Given that it occurs at a temperature between room temperature and $T = 100$ K, the thermodynamic signature of such a minor movement of the atoms would be virtually impossible to resolve using typical laboratory-based physical property probes such as specific heat. A more precise measurement of one of the elastic properties of the crystal would be needed to find the precise temperature of the phase transition or if the transition is continuous.

Since we have demonstrated that it is possible to synthesize CeGaGe crystals that remain in the body-centered structure down to 100 K using float zone refining, we can speculate that the structural transition observed in the flux-grown crystals is either due to small amounts of impurities or crystallographic defects in the flux-grown samples. Given the dependence on the physical properties of CeAlGe to precise stoichiometry [19,26,63,92], minor compositional variations could also be responsible for the symmetry change upon lowering temperature.

VI. CONCLUSIONS

The measurements presented in this paper definitively show that the candidate Weyl semimetal CeGaGe crystallizes with noncentrosymmetric $I4_1md$ symmetry at room temperature and, in some samples, remains in this symmetry at cryogenic temperatures. For those samples that show a structural transition, it is a transition to another noncentrosymmetric symmetry. This structural transition is extremely subtle. We do not observe it in measurements of the bulk thermodynamic properties, as it involves atomic displacements that are below the level expected from thermal contractions at these temperatures. A careful measurement of the temperature dependence of the elastic constants would be required to resolve the temperature of the phase transition.

With any quantum material, having high-quality samples is extremely important, but since the electronic band structure is intimately linked to the crystal structure and its symmetries, having high-quality, well-characterized samples is especially important for materials thought to host topologically protected states. As we emphasize in this paper, in the RXZ materials, a simple powder diffraction experiment is not enough. These experiments do not resolve differences between centrosymmetric and noncentrosymmetric structures. In CeGaGe, we clearly see a temperature-dependent change in crystal symmetry.

Given its compositional and structural similarities to other materials that host an interplay between exotic electronic states and magnetism, CeGaGe is an excellent candidate for study in this context. The strong magnetic anisotropy and possible signatures of multiple magnetic phases seen in measurements of the magnetic susceptibility in flux-grown crystals [69] suggest that it is likely that there will be rich magnetic phenomena in CeGaGe, which can now be understood definitively with respect to the crystal structure. Given the strong sensitivity of the physical properties to precise stoichiometry in related CeAlGe [26] and the structural transitions discussed in Sec. V, caution should be used in interpreting CeGaGe measurements. However, now that the structure is known, any future measurements and calculations of electronic structure are on much firmer footing, both in the broad context of magnetic Weyl semimetals and in the narrower context of CeGaGe specifically.

ACKNOWLEDGMENTS

W.J.G. would like to acknowledge helpful conversations with C. Huang and J. Brill about these experiments. The D8 Venture diffractometer was funded by the National Science Foundation Major Research Instrumentation Award (NSF-CHE-1625732) and by the University of Kentucky.

- [1] M. Z. Hasan and C. L. Kane, *Colloquium: Topological insulators*, *Rev. Mod. Phys.* **82**, 3045 (2010).
 [2] A. H. Castro Neto, F. Guinea, N. M. R. Peres, K. S. Novoselov, and A. K. Geim, The electronic properties of graphene, *Rev. Mod. Phys.* **81**, 109 (2009).

- [3] E. Y. Andrei and A. H. MacDonald, Graphene bilayers with a twist, *Nat. Mater.* **19**, 1265 (2020).
 [4] B. Yan and C. Felser, Topological materials: Weyl semimetals, *Annu. Rev. Condens. Matter Phys.* **8**, 337 (2017).

- [5] M. Z. Hasan, G. Chang, I. Belopolski, G. Bian, S.-Y. Xu, and J.-X. Yin, Weyl, Dirac and high-fold chiral fermions in topological quantum matter, *Nat. Rev. Mater.* **6**, 784 (2021).
- [6] N. P. Armitage, E. J. Mele, and A. Vishwanath, Weyl and Dirac semimetals in three-dimensional solids, *Rev. Mod. Phys.* **90**, 015001 (2018).
- [7] I. Belopolski *et al.*, Discovery of topological Weyl fermion lines and drumhead surface states in a room temperature magnet, *Science* **365**, 1278 (2019).
- [8] S.-Y. Xu *et al.*, Discovery of Lorentz-violating type II Weyl fermions in LaAlGe, *Sci. Adv.* **3**, e1603266 (2017).
- [9] Y.-M. Xie, X.-J. Gao, X. Y. Xu, C.-P. Zhang, J.-X. Hu, J. Z. Gao, and K. T. Law, Kramers nodal line metals, *Nat. Commun.* **12**, 3064 (2021).
- [10] M. M. Hirschmann, A. Leonhardt, B. Kilic, D. H. Fabini, and A. P. Schnyder, Symmetry-enforced band crossings in tetragonal materials: Dirac and Weyl degeneracies on points, lines, and planes, *Phys. Rev. Mater.* **5**, 054202 (2021).
- [11] J. Gaudet, H.-Y. Yang, S. Baidya, B. Lu, G. Xu, Y. Zhao, J. A. Rodriguez-Rivera, C. M. Hoffmann, D. E. Graf, D. H. Torchinsky *et al.*, Weyl-mediated helical magnetism in NdAlSi, *Nat. Mater.* **20**, 1650 (2021).
- [12] J.-F. Wang, Q.-X. Dong, Z.-P. Guo, M. Lv, Y.-F. Huang, J.-S. Xiang, Z.-A. Ren, Z.-J. Wang, P.-J. Sun, G. Li *et al.*, NdAlSi: A magnetic Weyl semimetal candidate with rich magnetic phases and atypical transport properties, *Phys. Rev. B* **105**, 144435 (2022).
- [13] J.-F. Wang, Q.-X. Dong, Y.-F. Huang, Z.-S. Wang, Z.-P. Guo, Z.-J. Wang, Z.-A. Ren, G. Li, P.-J. Sun, X. Dai *et al.*, Quantum oscillations in the magnetic Weyl semimetal NdAlSi arising from strong Weyl fermion- $4f$ electron exchange interaction, *Phys. Rev. B* **108**, 024423 (2023).
- [14] C. Li, J. Zhang, Y. Wang, H. Liu, Q. Guo, E. Rienks, W. Chen, F. Bertran, H. Yang, D. Phuyal *et al.*, Emergence of Weyl fermions by ferrimagnetism in a noncentrosymmetric magnetic Weyl semimetal, *Nat. Commun.* **14**, 7185 (2023).
- [15] P. K. Tanwar, M. Ahmad, M. S. Alam, X. Yao, F. Tafti, and M. Matusiak, Gravitational anomaly in the ferrimagnetic topological Weyl semimetal NdAlSi, *Phys. Rev. B* **108**, L161106 (2023).
- [16] Q.-X. Dong, J.-F. Wang, L.-B. Zhang, J.-L. Bai, Q.-Y. Liu, J.-W. Cheng, P.-Y. Liu, C.-D. Li, J.-S. Xiang, Z.-A. Ren *et al.*, Large power factor, anomalous Nernst effect, and temperature-dependent thermoelectric quantum oscillations in the magnetic Weyl semimetal NdAlSi, *Phys. Rev. B* **108**, 205143 (2023).
- [17] K. Cho, W. H. Shon, K. Kim, J. Bae, J. Lee, C.-S. Park, S. Yoon, B. Cho, P. Rawat, and J.-S. Rhyee, Anisotropic metamagnetic transition and intrinsic Berry curvature in magnetic Weyl semimetal NdAlGe, *SSRN* (2022).
- [18] X. He, Y. Li, H. Zeng, Z. Zhu, S. Tan, Y. Zhang, C. Cao, and Y. Luo, Pressure-tuning domain-wall chirality in noncentrosymmetric magnetic Weyl semimetal CeAlGe, *Sci. China Phys. Mech. Astron.* **66**, 237011 (2023).
- [19] H. Hodovanets, C. J. Eckberg, P. Y. Zavalij, H. Kim, W.-C. Lin, M. Zic, D. J. Campbell, J. S. Higgins, and J. Paglione, Single-crystal investigation of the proposed type-II Weyl semimetal CeAlGe, *Phys. Rev. B* **98**, 245132 (2018).
- [20] H. Hodovanets, C. J. Eckberg, D. J. Campbell, Y. Eo, P. Y. Zavalij, P. Piccoli, T. Metz, H. Kim, J. S. Higgins, and J. Paglione, Anomalous symmetry breaking in the Weyl semimetal CeAlGe, *Phys. Rev. B* **106**, 235102 (2022).
- [21] M. M. Piva, J. C. Souza, G. A. Lombardi, K. R. Pakuszewski, C. Adriano, P. G. Pagliuso, and M. Nicklas, Topological Hall effect in CeAlGe, *Phys. Rev. Mater.* **7**, 074204 (2023).
- [22] P. Puphal, V. Pomjakushin, N. Kanazawa, V. Ukleev, D. J. Gawryluk, J. Ma, M. Naamneh, N. C. Plumb, L. Keller, R. Cubitt *et al.*, Topological magnetic phase in the candidate Weyl semimetal CeAlGe, *Phys. Rev. Lett.* **124**, 017202 (2020).
- [23] T. Suzuki, L. Savary, J.-P. Liu, J. W. Lynn, L. Balents, and J. G. Checkelsky, Singular angular magnetoresistance in a magnetic nodal semimetal, *Science* **365**, 377 (2019).
- [24] N. C. Drucker *et al.*, Topology stabilized fluctuations in a magnetic nodal semimetal, *Nat. Commun.* **14**, 5182 (2023).
- [25] Z. Wang, X. He, F. Lu, H. Zeng, S. Zou, X.-X. Zhang, and Y. Luo, ^{27}Al NMR study of the magnetic Weyl semimetal CeAlGe, *Phys. Rev. B* **109**, 245106 (2024).
- [26] P. Puphal, C. Mielke, N. Kumar, Y. Soh, T. Shang, M. Medarde, J. S. White, and E. Pomjakushina, Bulk single-crystal growth of the theoretically predicted magnetic Weyl semimetals RAlGe ($R = \text{Pr}, \text{Ce}$), *Phys. Rev. Mater.* **3**, 024204 (2019).
- [27] M. S. Alam, A. Fakhredine, M. Ahmad, P. K. Tanwar, H.-Y. Yang, F. Tafti, G. Cuono, R. Islam, B. Singh, A. Lynnyk *et al.*, Sign change of anomalous Hall effect and anomalous Nernst effect in the Weyl semimetal CeAlSi, *Phys. Rev. B* **107**, 085102 (2023).
- [28] C. Tzschaschel *et al.*, Nonlinear optical diode effect in a magnetic Weyl semimetal, *Nat. Commun.* **15**, 3017 (2024).
- [29] E. Cheng *et al.*, Tunable positions of Weyl nodes via magnetism and pressure in the ferromagnetic Weyl semimetal CeAlSi, *Nat. Commun.* **15**, 1467 (2024).
- [30] M. M. Piva, J. C. Souza, V. Brousseau-Couture, S. Sorn, K. R. Pakuszewski, J. K. John, C. Adriano, M. Côté, P. G. Pagliuso, A. Paramakanti *et al.*, Topological features in the ferromagnetic Weyl semimetal CeAlSi: Role of domain walls, *Phys. Rev. Res.* **5**, 013068 (2023).
- [31] A. P. Sakhya, C.-Y. Huang, G. Dhakal, X.-J. Gao, S. Regmi, B. Wang, W. Wen, R.-H. He, X. Yao, R. Smith *et al.*, Observation of Fermi arcs and Weyl nodes in a noncentrosymmetric magnetic Weyl semimetal, *Phys. Rev. Mater.* **7**, L051202 (2023).
- [32] Y. Sun, C. Lee, H.-Y. Yang, D. H. Torchinsky, F. Tafti, and J. Orenstein, Mapping domain-wall topology in the magnetic Weyl semimetal CeAlSi, *Phys. Rev. B* **104**, 235119 (2021).
- [33] B. Xu, J. Franklin, A. Jayakody, H. Yang, F. Tafti, and I. Sochnikov, Picoscale magnetoelasticity governs heterogeneous magnetic domains in a noncentrosymmetric ferromagnetic Weyl semimetal, *Adv. Quantum Technol.* **4**, 2000101 (2021).
- [34] H.-Y. Yang *et al.*, Noncollinear ferromagnetic Weyl semimetal with anisotropic anomalous Hall effect, *Phys. Rev. B* **103**, 115143 (2021).
- [35] A. Laha, A. K. Kundu, N. Aryal, E. S. Bozin, J. Yao, S. Paone, A. Rajapitamahuni, E. Vescovo, T. Valla, M. Abeykoon *et al.*, Electronic structure and magnetic and transport properties of antiferromagnetic Weyl semimetal GdAlSi, *Phys. Rev. B* **109**, 035120 (2024).
- [36] P. Meena, A. Choudhury, M. Mudgal, S. Bagga, V. K. Tiwari, S. Rajput, C. S. Yadav, V. K. Malik, T. Maitra, and J. Nayak, Exploration of quantum oscillation in antiferromagnetic Weyl semimetal GdSiAl, *J. Phys.: Condens. Matter* **37**, 065704 (2024).

- [37] W. Cao, N. Zhao, C. Pei, Q. Wang, Q. Zhang, T. Ying, Y. Zhao, L. Gao, C. Li, N. Yu *et al.*, Pressure-induced superconductivity in the noncentrosymmetric Weyl semimetals LaAlX ($X = \text{Si, Ge}$), *Phys. Rev. B* **105**, 174502 (2022).
- [38] T. Ng, Y. Luo, J. Yuan, Y. Wu, H. Yang, and L. Shen, Origin and enhancement of the spin Hall angle in the Weyl semimetals LaAlSi and LaAlGe, *Phys. Rev. B* **104**, 014412 (2021).
- [39] I. Kim, B. Kang, H. Kim, and M. Choi, Crystallographic defects in Weyl semimetal LaAlGe, *Phys. Rev. Mater.* **8**, 054203 (2024).
- [40] C. Dhital, R. L. Dally, R. Ruvalcaba, R. Gonzalez-Hernandez, J. Guerrero-Sanchez, H. B. Cao, Q. Zhang, W. Tian, Y. Wu, M. D. Frontzek *et al.*, Multi- k magnetic structure and large anomalous Hall effect in candidate magnetic Weyl semimetal NdAlGe, *Phys. Rev. B* **107**, 224414 (2023).
- [41] N. Kikugawa, T. Terashima, T. Kato, M. Hayashi, H. Yamaguchi, and S. Uji, Bulk physical properties of a magnetic Weyl semimetal candidate NdAlGe grown by a laser floating-zone method, *Inorganics* **11**, 20 (2023).
- [42] T. Wang, Y. Guo, C. Wang, and S. Yang, Correlation between non-centrosymmetric structure and magnetic properties in Weyl semimetal NdAlGe, *Solid State Commun.* **321**, 114041 (2020).
- [43] H.-Y. Yang, J. Gaudet, R. Verma, S. Baidya, F. Bahrami, X. Yao, C.-Y. Huang, L. DeBeer-Schmitt, A. A. Aczel, G. Xu *et al.*, Stripe helical magnetism and two regimes of anomalous Hall effect in NdAlGe, *Phys. Rev. Mater.* **7**, 034202 (2023).
- [44] J. Zhao, W. Liu, A. Rahman, F. Meng, L. Ling, C. Xi, W. Tong, Y. Bai, Z. Tian, Y. Zhong *et al.*, Field-induced tricritical phenomenon and magnetic structures in magnetic Weyl semimetal candidate NdAlGe, *New J. Phys.* **24**, 013010 (2022).
- [45] N. Kikugawa, S. Uji, and T. Terashima, Anomalous Hall effect in the magnetic Weyl semimetal NdAlGe with plateaus observed at low temperatures, *Phys. Rev. B* **109**, 035143 (2024).
- [46] D. Destraz, L. Das, S. S. Tsirkin, Y. Xu, T. Neupert, J. Chang, A. Schilling, A. G. Grushin, J. Kohlbrecher, L. Keller *et al.*, Magnetism and anomalous transport in the Weyl semimetal PrAlGe: Possible route to axial gauge fields, *npj Quantum Mater.* **5**, 5 (2020).
- [47] B. Meng, H. Wu, Y. Qiu, C. Wang, Y. Liu, Z. Xia, S. Yuan, H. Chang, and Z. Tian, Large anomalous Hall effect in ferromagnetic Weyl semimetal candidate PrAlGe, *APL Mater.* **7**, 051110 (2019).
- [48] D. S. Sanchez, G. Chang, I. Belopolski, H. Lu, J.-X. Yin, N. Alidoust, X. Xu, T. A. Cochran, X. Zhang, Y. Bian *et al.*, Observation of Weyl fermions in a magnetic non-centrosymmetric crystal, *Nat. Commun.* **11**, 3356 (2020).
- [49] R. Yang, M. Corasaniti, C. C. Le, C. Yue, Z. Hu, J. P. Hu, C. Petrovic, and L. Degiorgi, Charge dynamics of a noncentrosymmetric magnetic Weyl semimetal, *npj Quantum Mater.* **7**, 101 (2022).
- [50] K. Shoriki, K. Moriishi, Y. Okamura, K. Yokoi, H. Usui, H. Murakawa, H. Sakai, N. Hanasaki, Y. Tokura, and Y. Takahashi, Large nonlinear optical magnetoelectric response in a noncentrosymmetric magnetic Weyl semimetal, *Proc. Natl. Acad. Sci. USA* **121**, e2316910121 (2024).
- [51] H.-Y. Yang, B. Singh, B. Lu, C.-Y. Huang, F. Bahrami, W.-C. Chiu, D. Graf, S.-M. Huang, B. Wang, H. Lin *et al.*, Transition from intrinsic to extrinsic anomalous Hall effect in the ferromagnetic Weyl semimetal PrAlGe $_{1-x}$ Si $_x$, *APL Mater.* **8**, 011111 (2020).
- [52] M. Lyu, J. Xiang, Z. Mi, H. Zhao, Z. Wang, E. Liu, G. Chen, Z. Ren, G. Li, and P. Sun, Nonsaturating magnetoresistance, anomalous Hall effect, and magnetic quantum oscillations in the ferromagnetic semimetal PrAlSi, *Phys. Rev. B* **102**, 085143 (2020).
- [53] L. Wu, S. Chi, H. Zuo, G. Xu, L. Zhao, Y. Luo, and Z. Zhu, Field-induced Lifshitz transition in the magnetic Weyl semimetal candidate PrAlSi, *npj Quantum Mater.* **8**, 4 (2023).
- [54] R. Lou, A. Fedorov, L. Zhao, A. Yaresko, B. Büchner, and S. Borisenko, Signature of weakly coupled f electrons and conduction electrons in magnetic Weyl semimetal candidates PrAlSi and SmAlSi, *Phys. Rev. B* **107**, 035158 (2023).
- [55] X. Yao, J. Gaudet, R. Verma, D. E. Graf, H.-Y. Yang, F. Bahrami, R. Zhang, A. A. Aczel, S. Subedi, D. H. Torchinsky *et al.*, Large topological Hall effect and spiral magnetic order in the Weyl semimetal SmAlSi, *Phys. Rev. X* **13**, 011035 (2023).
- [56] W. Cao, Y. Su, Q. Wang, C. Pei, L. Gao, Y. Zhao, C. Li, N. Yu, J. Wang, Z. Liu *et al.*, Quantum oscillations in noncentrosymmetric Weyl semimetal SmAlSi, *Chin. Phys. Lett.* **39**, 047501 (2022).
- [57] L. Xu, H. Niu, Y. Bai, H. Zhu, S. Yuan, X. He, Y. Han, L. Zhao, Y. Yang, Z. Xia *et al.*, Shubnikov–de Haas oscillations and nontrivial topological states in Weyl semimetal candidate SmAlSi, *J. Phys.: Condens. Matter* **34**, 485701 (2022).
- [58] J. Gong, H. Wang, K. Han, X.-Y. Zeng, X.-P. Ma, Y.-T. Wang, J.-F. Lin, X.-Y. Wang, and T.-L. Xia, Anomalous Hall effect in an antiferromagnetic CeGaSi single crystal, *Phys. Rev. B* **109**, 024434 (2024).
- [59] H. Lu, W. Yang, Y. Huang, Y. Bian, X. Zhang, and S. Jia, Multi-experimental determination of magnetic transition in Weyl semimetals RAlGe, *Mater. Lett.* **335**, 133819 (2023).
- [60] J. Bouaziz, G. Bihlmayer, C. E. Patrick, J. B. Staunton, and S. Blügel, Origin of incommensurate magnetic order in the RAlSi magnetic Weyl semimetals ($R = \text{Pr, Nd, Sm}$), *Phys. Rev. B* **109**, L201108 (2024).
- [61] H. Lu, H. Zang, X. Ren, X. He, V. Rodionova, E. Yan, and K. Magomedov, Comparative analysis of magnetoresistance in Weyl semimetal RAlSi, *J. Mater. Sci.* **59**, 14653 (2024).
- [62] J. T. Zhao and E. Parthé, Structure of YAlGe and isotypic rare-earth–aluminium germanides, *Acta Cryst. C* **46**, 2276 (1990).
- [63] S. Dhar, S. Pattalwar, and R. Vijayaraghavan, Magnetic and thermal behavior of CeAlX ($X = \text{Si and Ge}$) compounds, *J. Magn. Magn. Mater.* **104–107**, 1303 (1992).
- [64] W. He, J. Zhang, L. Zeng, and Y. Zhuang, Crystal structural refinement for NdAlSi, *Rare Metals* **25**, 355 (2006).
- [65] P. J. Brown, A. G. Fox, E. N. Maslen, M. A. O’Keefe, and B. T. M. Willis, Intensity of diffracted intensities, in *International Tables for Crystallography Volume C: Mathematical, Physical and Chemical Tables*, edited by E. Prince (Springer, Dordrecht, 2006), pp. 554–595.
- [66] Y. Grin, P. Rogl, B. Chevalier, A. Fedorchuk, and I. Gryniv, Physical properties of binary cerium gallides and ternary cerium–germanium gallides, *J. Less-Common Met.* **167**, 365 (1991).
- [67] R. Pöttgen and B. Chevalier, Equiatomic cerium intermetallics CeXX’ with two p elements, *Z. Naturforsch. B* **70**, 695 (2015).
- [68] S. Dhar, S. Pattalwar, and R. Vijayaraghavan, CeGeGa—A ferromagnetic dense Kondo system, *Phys. B: Condens. Matter* **186–188**, 491 (1993).

- [69] D. Ram, S. Malick, Z. Hossain, and D. Kaczorowski, Magnetic, thermodynamic, and magnetotransport properties of CeGaGe and PrGaGe single crystals, *Phys. Rev. B* **108**, 024428 (2023).
- [70] H. M. Rietveld, A profile refinement method for nuclear and magnetic structures, *J. Appl. Cryst.* **2**, 65 (1969).
- [71] V. F. Sears, Neutron scattering lengths and cross sections, *Neutron News* **3**, 26 (1992).
- [72] Neutron scattering lengths and cross sections (2021), <https://www.ncnr.nist.gov/resources/n-lengths/> [Accessed 16-07-2024].
- [73] See Supplemental Material at <http://link.aps.org/supplemental/10.1103/PhysRevB.111.184102> for details of EDX, PXRD, and SCXRD; further verification of SCND data quality; and the quality of the data where $10^{-4} \leq |F_c|^2 \leq 1.25$ for the $I4_1/amd$ model.
- [74] P. Statham, Digital pulse processing and pile up correction for accurate interpretation of high rate SDD spectrum images, *Microsc. Microanal.* **13**, 1428 (2007).
- [75] J. Rodríguez-Carvajal, Recent advances in magnetic structure determination by neutron powder diffraction, *Phys. B: Condens. Matter* **192**, 55 (1993).
- [76] M. I. Aroyo, H. Burzlaff, G. Chapuis, W. Fischer, H. D. Flack, A. M. Glazer, H. Grimmer, B. Gruber, Th. Hahn, H. Klapper, E. Koch, P. Konstantinov, V. Kopský, D. B. Litvin, A. Looijenga-Vos, K. Momma, U. Müller, U. Shmueli, B. Souvignier, J. C. H. Spence *et al.*, in *International Tables for Crystallography Volume A: Space-Group Symmetry*, edited by M. I. Aroyo (International Union of Crystallography, Chester, 2016), Chap. 2.3.
- [77] L. Coates, H. B. Cao, B. C. Chakoumakos, M. D. Frontzek, C. Hoffmann, A. Y. Kovalevsky, Y. Liu, F. Meilleur, A. M. dos Santos, D. A. A. Myles *et al.*, A suite-level review of the neutron single-crystal diffraction instruments at Oak Ridge National Laboratory, *Rev. Sci. Instrum.* **89**, 092802 (2018).
- [78] F. Akeroyd *et al.*, MANTID: Manipulation and analysis toolkit for instrument data (2013), <https://www.mantidproject.org/>.
- [79] R. Applin, R. Baust, A. Diaz-Alvarez, C. Finn, S. Foxley, J. Haigh, T. Hampson, and P. F. Peterson, *MANTID 6.9.1: Manipulation and analysis toolkit for instrument data* (2024), doi:10.5286/Software/Mantid6.9.1.
- [80] B. H. Toby and R. B. Von Dreele, GSAS-II: The genesis of a modern open-source all purpose crystallography software package, *J. Appl. Cryst.* **46**, 544 (2013).
- [81] S. F. Mughabghab, Thermal cross sections, in *Atlas of Neutron Resonances: Resonance Parameters and Thermal Cross Sections Z = 1–100* (Elsevier, Amsterdam, 2018), pp. 1–16.
- [82] Thermal neutron resonances, <https://www.ncnr.nist.gov/resources/activation/resonance.html>, [Accessed 14-11-2024].
- [83] Bruker AXS Inc., APEX3, SAINT, and SADABS, Madison, WI, USA (2016).
- [84] L. Krause, R. Herbst-Irmer, and D. Stalke, An empirical correction for the influence of low-energy contamination, *J. Appl. Crystallogr.* **48**, 1907 (2015).
- [85] G. M. Sheldrick, SHELXT—Integrated space-group and crystal-structure determination, *Acta Crystallogr. A* **71**, 3 (2015).
- [86] G. M. Sheldrick, Crystal structure refinement with SHELXL, *Acta Crystallogr. C* **71**, 3 (2015).
- [87] H. D. Flack, On enantiomorph-polarity estimation, *Acta Crystallogr. A* **39**, 876 (1983).
- [88] F. Wöhler and H. S. Deville, Ueber das Bor, *Liebigs Ann.* **101**, 347 (1857).
- [89] P. C. Canfield and Z. Fisk, Growth of single crystals from metallic fluxes, *Philos. Mag. B* **65**, 1117 (1992).
- [90] Á. Valentín-Pérez, P. Rosa, E. A. Hillard, and M. Giorgi, Chirality determination in crystals, *Chirality* **34**, 163 (2022).
- [91] S. Parsons, Determination of absolute configuration using x-ray diffraction, *Tetrahedron: Asymmetry* **28**, 1304 (2017).
- [92] H. Flandorfer, D. Kaczorowski, J. Gröbner, P. Rogl, R. Wouters, C. Godart, and A. Kostikas, The systems Ce–Al–(Si, Ge): Phase equilibria and physical properties, *J. Solid State Chem.* **137**, 191 (1998).